

# Microstructure engineering of polyamide membranes for ultrafast polar and non-polar solvent transport

Received: 10 February 2025

Accepted: 19 August 2025

Published online: 25 September 2025

Huiqing Wu<sup>1,2</sup>✉, Yang Xu<sup>1</sup>, Qingchen Tang<sup>3</sup>, Baohu Wu<sup>1,4</sup> & Peiyi Wu<sup>1</sup>✉

Highly permselective membranes with superior permeability and broad applicability are essential for organic solvent nanofiltration (OSN). However, conventional polyamide membranes often suffer from limited permeability, especially for non-polar solvents. We herein propose a simple yet effective strategy to fabricate polyamide membranes capable of ultrafast separation for both polar and non-polar solvents. By utilizing a non-planar amine monomer with diphenyl ether moiety, interfacial polymerization is rationally conducted at the deep eutectic solvent/alkane interface, yielding an ultrathin polyamide layer (~12 nm) with enhanced microporosity, uniform nanopores and a Janus-like microstructure. The resultant membrane demonstrates high permeability (36.6 L m<sup>-2</sup> h<sup>-1</sup> bar<sup>-1</sup> for methanol, 56.6 L m<sup>-2</sup> h<sup>-1</sup> bar<sup>-1</sup> for hexane), precise molecular sieving capability and excellent structural stability. The work provides a paradigm for developing high-performance OSN membranes through the molecular-level design and powerful control of the manufacturing process.

Organic solvent nanofiltration (OSN) has gained significant attention across diverse industries such as the petroleum, chemicals and pharmaceuticals, due to its advantages in energy conservation and operational simplicity. OSN membranes are designed to effectively separate small molecules (150–1000 Da) from organic solvents through size-exclusion and charge-repulsion mechanism. In industrial applications involving large volumes of aggressive organic solvents, there is an urgent demand for OSN membranes with high separation efficiency and robust stability under complex conditions, particularly in organic solvents spanning a wide polarity range<sup>1–3</sup>.

Thin film composite (TFC) membrane, consisting of a porous substrate and a selective thin layer formed through interfacial polymerization (IP), represents the mainstream in OSN membranes, owing to the merits of industrially scale-up and cost-effective production<sup>4</sup>. Polyamide (PA) TFC membranes, as a primary type, are typically fabricated via the interfacial polymerization between diamine (e.g., m-phenylenediamine, MPD) and triacyl chloride (e.g., trimesoyl chloride,

TMC) at a water/alkane interface. However, conventional PA membranes often suffer limited permeability for organic solvents, especially poor performance for non-polar solvents, probably as a result of the hydrophilic and dense polyamide structures<sup>2,5–7</sup>.

To enhance OSN performance of PA TFC membranes, several strategies have been developed. On the one hand, introducing hydrophobic groups to the amine monomers or using macrocyclic monomers with hydrophobic cavities can increase the hydrophobicity of the resulting PA network, thereby facilitating the passage of non-polar solvents<sup>6,8–12</sup>. On the other hand, employing contorted aromatic amines, macrocycles and organic cages as monomeric units can elevate the membrane's intrinsic microporosity, promoting rapid solvent transport<sup>7,8,10,13–16</sup>. However, those unconventional amine monomers are often synthetically challenging and costly. Additionally, the variety of aromatic amines, particularly those with spatial geometries or with hydrophobic segments, is severely limited by their poor aqueous solubility. Another straightforward approach to improve membrane

<sup>1</sup>State Key Laboratory of Advanced Fiber Materials (Donghua University), College of Chemistry and Chemical Engineering, Donghua University, Shanghai, China. <sup>2</sup>National Innovation Center of Advanced Dyeing and Finishing Technology, Tai'an, Shandong, China. <sup>3</sup>State Key Laboratory of Advanced Fiber Materials (Donghua University), Center for Advanced Low-Dimension Materials, and College of Materials Sciences and Engineering, Donghua University, Shanghai, China. <sup>4</sup>Jülich Centre for Neutron Science (JCNS) at Heinz Maier-Leibnitz Zentrum (MLZ) Forschungszentrum Jülich, Garching, Germany.

✉ e-mail: [huiqingwu@dhu.edu.cn](mailto:huiqingwu@dhu.edu.cn); [wupeiyi@dhu.edu.cn](mailto:wupeiyi@dhu.edu.cn)

permeance is to thin the polyamide layer by controlling the interfacial polymerization process<sup>1,17</sup>. Nevertheless, in conventional water/alkane interfacial systems, uncontrolled monomer diffusion, rapid polymerization and the inevitable hydrolysis of acyl chloride, easily lead to the formation of a thick and heterogeneous PA layer, ultimately compromising both membrane permeability and selectivity.

To address these current challenges, we herein propose a comprehensive three-in-one strategy to engineer a well-structured polyamide architecture that simultaneously achieves the high permeability for both polar and non-polar solvents, while maintaining effective molecular sieving. This strategy features three notable aspects: (i) Equipping diamine monomer with diphenyl ether moiety, fosters a balance between the hydrophilic and hydrophobic domains within the polyamide layer. It creates Janus-like dual pathways—one preferential for polar solvents and the other for nonpolar solvents, enabling efficient permeation of organic solvents across a broad polarity spectrum. (ii) Incorporating contorted unit into polyamide backbone enhances intrinsic microporosity and interconnectivity, which promotes the solvent permeability. (iii) Exploring deep eutectic solvent (DES) as a substitute for water, not only allows the utilization of non-water-soluble amine monomers, but also fine-tunes the interfacial properties and reaction environment in an anhydrous system, leading to effective control over the IP process. The distinctive characteristics of this approach facilitate the formation of TFC membranes with ultrathin, highly microporous, and Janus-like polyamide layers.

The as-prepared membrane demonstrates excellent transport performance across wide range of solvent polarities, outperforming most existing OSN membranes. The membrane also displays a sharp molecular weight cutoff and precise molecular separation capability. This work establishes a new benchmark for the molecular-level design and engineering of OSN membranes, paving the way for a broad spectrum of applications.

## Results

### Membrane design and characterization

Primarily, 4,4'-diaminodiphenyl ether (ODA), was rationally selected as molecular building block for polyamide OSN membrane based on its unique structural and chemical properties as follows. As depicted in Fig. 1a, ODA adopts a spiral conformation with a plane angle of 113.6°. The high reactivity of amide groups on ODA is evidenced by the similar electrostatic potential (ESP) value of N atom with that of MPD (Supplementary Fig. 1)<sup>18</sup>. Despite these favorable characteristics that make ODA a promising amine monomer candidate, ODA has not yet been used in conventional alkane/water interfacial polymerization due to poor water solubility.

In particular, a DES formed from choline chloride and ethylene glycol, was judiciously selected as the solvent of amine monomer replacing water in the interfacial polymerization system. Firstly, the DES exhibits favorable properties including facile preparation, biodegradability, cost-effectiveness, and excellent solubility for water-insoluble ODA monomer. Secondly, the DES solution is capable of forming a sharp and stable interface with cyclohexane. Note that, the interfacial polymerization occurs at the DES side, due to the predominant diffusion of TMC from cyclohexane to DES phase, as determined by the calculated partition coefficient of ODA and TMC between the immiscible DES and cyclohexane phases (Supplementary Table 1). This indicates that, it presents an opposite monomer diffusion direction and reaction position, contrasting with the conventional alkane/water interfacial system, where amine diffusion dominates and interfacial polymerization occurs at the alkane side. Thirdly, the inherent physicochemical properties of DES including its relative high viscosity (17.3 mPa·s) and low surface tension, help to restrain the Marangoni effect at the interface and endue high DES/cyclohexane interfacial stability (Supplementary Table 2). The molecular dynamics simulation results (Supplementary Fig. 2a–c) suggest that the diffusion

rate of ODA monomer in DES could be effectively retarded, due to the synergetic effect of DES's high viscosity and the strong hydrogen bonding interaction between ODA and DES. Moreover, the anhydrous nature of this system completely eliminates the side reaction of acyl chloride hydrolysis. These distinctive features of the DES/cyclohexane system confer the great potential in maneuverability of IP process and the resulting PA structure.

To visualize the IP process between ODA and TMC, ODA/DES solution (1%) was kept in contact with TMC/cyclohexane solution (0.15%) in a glass bottle, and a freestanding nanofilm was generated at the interface of two phases (Fig. 1c). The characteristic peaks at 1648 cm<sup>-1</sup>, ascribed to the stretching vibration of amide groups (–CO–NH–), is found in FTIR spectrum of the product from the polymerization between ODA and TMC (ODA/TMC) (Supplementary Fig. 3), suggesting the successful formation of polyamide through polycondensation between ODA and TMC. By simply adjusting IP reaction time to 75 s, the resulting ODA/TMC nanofilm achieves an ultra-thin thickness of ~12 nm, observed from AFM image of Fig. 1d.

In Fig. 1e, the SAXS results of ODA/TMC nanofilm reveals a hierarchical structure characterized by three distinct scattering regimes. This scattering pattern demonstrates the coexistence of an overall dense polyamide network framework with uniformly distributed phase-separated domains at different length scales. Particularly, the intermediate *q*-range (3–7 nm<sup>-1</sup>) exhibits a broad scattering peak centered at *q* ≈ 5 nm<sup>-1</sup>, which is attributed to nanoscale phase separation within the amorphous regions of the PA matrix. Through analysis the data using the Teubner–Strey model, the periodicity of the phase-separated domains (*d* ≈ 1.3 nm), and the correlation length ( $\xi$  ≈ 0.8 nm) were obtained, representing the average distance of the nanochannel<sup>19</sup>.

As the results of CO<sub>2</sub> adsorption isotherms shown in Fig. 1f, the accessible surface area of ODA/TMC nanofilm is 222 m<sup>2</sup> g<sup>-1</sup>, appropriately two times higher than that of MPD/TMC nanofilm (72.8 m<sup>2</sup> g<sup>-1</sup>). Besides, the elongated moiety (phenyl oxide) leads to a larger pore size of ODA/TMC than that MPD/TMC network (Supplementary Fig. 4). Molecular dynamics simulations were employed to demonstrate the structural models of polyamide from different amine monomers. As shown in Fig. 1g, the fractional free volume (FFV, blue region) of ODA/TMC and MPD/TMC network is 33.8% and 19.8%, respectively. In addition to extra free volume, higher interconnectivity between the free volume units could also be found in ODA/TMC structure. Analysis probes with different radii also confirm the higher porosity of ODA/TMC structure (Fig. 1h). Those characterization and simulation verify the enhancement of interconnected microporous architecture of PA made from ODA and TMC, as a result of the contorted ODA monomer restraining the dense packing of polymer segment.

The interfacial polymerization of ODA and TMC was subsequently conducted on the surface of Nylon substrate for a reaction time of 75 s, resulting in a ODA/TMC TFC membrane. A dense and defect-free nanofilm is observed to cover on top of Nylon porous substrate, and the nanofilm is so thin that it preserves the underlying undulate morphology of the substrate (Fig. 2a, b). The thickness of PA layer is approximately a dozen nanometers from the cross-sectional SEM and TEM images (Fig. 2c, d). Figure 2e demonstrates the membrane's high wettability towards various organic solvents, derived from the small contact angles of below 25° for polar solvents and especially below 10° for non-polar solvents. Meanwhile, the water contact angle of ~89° suggest the relative hydrophobicity of the membrane, which arises from the incorporation of diphenyl ether-containing ODA monomers into the polyamide network. Moreover, as presented in Fig. 2f, the Zisman plot of solvent-membrane contact angles provides the critical surface tension of the membrane ( $\gamma_c$  = 21.7 mN m<sup>-1</sup>), defining the wetting threshold for the ODA/TMC membrane. The solvent fluid is predicted to completely wet the membrane, when its surface tension is smaller than  $\gamma_c$ . For ODA/TMC membrane, the strong affinity towards

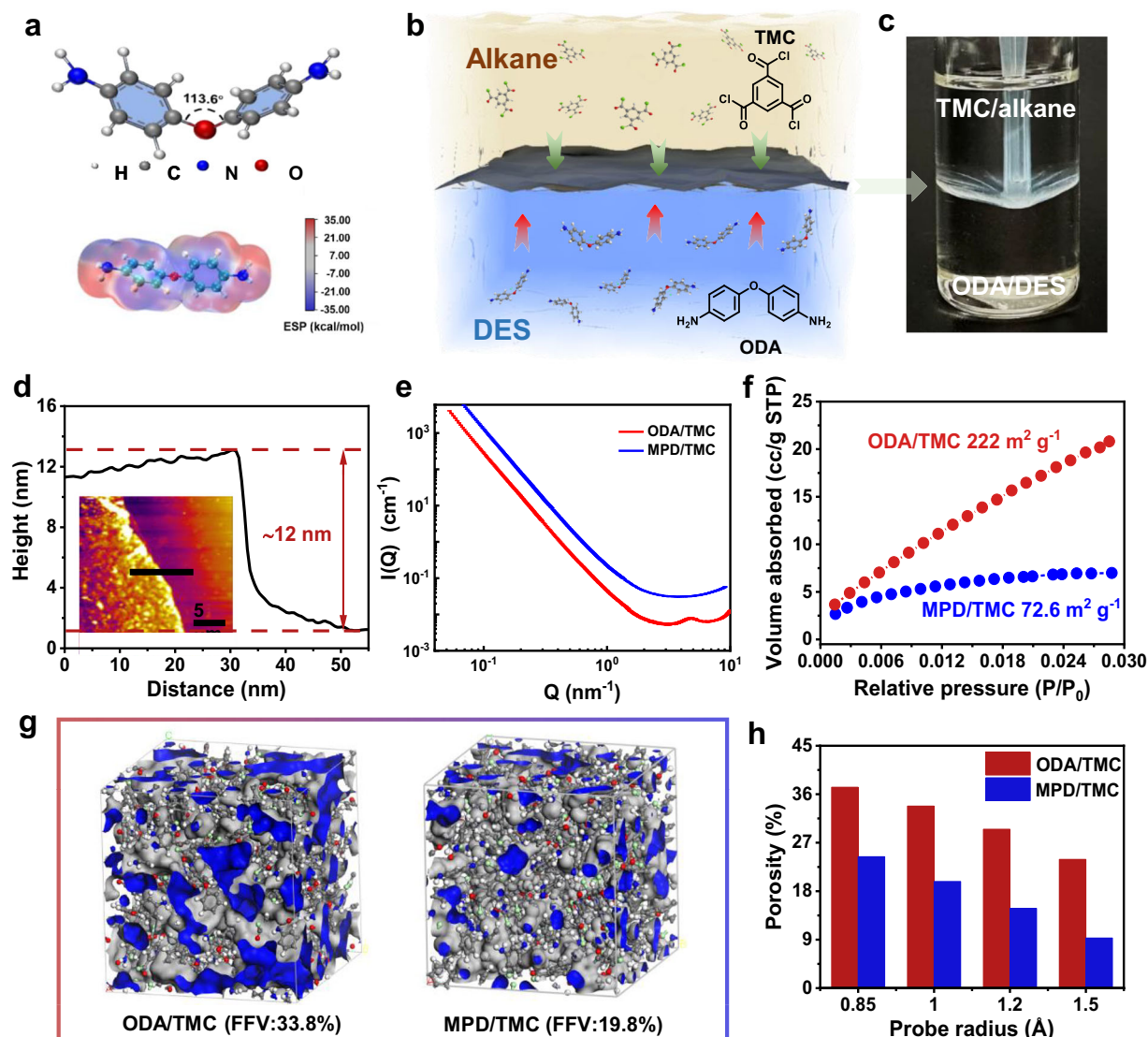


**Fig. 1 | ODA/TMC membrane formation and characterization.** **a** 3D conformation and distribution of electrostatic potential at the molecular van der Waals surface of ODA monomer. **b** Diagram of interfacial polymerization between TMC and ODA at the alkane/DES interface. **c** Photograph of the free-standing PA formed at alkanes/DES interface. **d** AFM image and corresponding height profile of the free-standing

ODA/TMC membrane. **e** SAXS Q-I plot in log-log scale of ODA/TMC and MPD/TMC in vacuum. **f** CO<sub>2</sub> absorption isotherms of ODA/TMC and MPD/TMC. **g** Molecular dynamics simulation of free volume of ODA/TMC and MPD/TMC network. **h** Porosities of ODA/TMC measured by different sizes of probes.

both polar and non-polar solvents favors the positive capillary force inside the pores, boosting the liquid transport<sup>20,21</sup>. The low  $\gamma_c$  value also reflects the membrane's hydrophobicity. In addition, the negatively-charged surface of the ODA/TMC TFC membrane was identified from the streaming potential value of -24.9 mV at pH = 7 (Supplementary Fig. 5). TGA analysis of ODA/TMC TFC membrane shows the excellent thermal stability up to 380 °C under nitrogen atmosphere (Supplementary Fig. 6).

### Nanofiltration performance of the membrane

Interfacial polymerization parameters were modulated to optimize ODA/TMC TFC membrane, and its performance in OSN was comprehensively evaluated. The reaction time for IP process plays a crucial role on the morphologies and performance of the TFC membrane (Fig. 3a, Supplementary Fig. 7). When the reaction time prolongs to 75 s, the permeance of the membrane for both methanol and cyclohexane decreases, while the rejection of RB19 reaches to 94.4%. With a further increase in reaction time, the RB19 rejection

almost maintains, whereas the solvent permeance continues to drop. The results suggest the growth in crosslinking degree of the resulted PA network at the initial stage of interfacial reaction, while the thickness of the PA layer predominantly increases rather than crosslinking degree, with extended reaction time (>75 s). Based on the N1s spectra of XPS analysis (Supplementary Fig. 8), according to the ratio of the peak of N-C=O (399.5 eV) to the whole, the percentage of the reacted -NH<sub>2</sub> group is estimated to be ~78%. The highly cross-linked PA network formed at 75 s could be attributed to the high reactivity of ODA monomer, the absence of the acyl chloride hydrolysis in the anhydrous interface, and the precise control of monomer diffusion and interfacial reaction kinetics. Increasing ODA concentration leads to the formation of ODA/TMC TFC membrane with lower permeance and higher dye rejection, and the dye rejection achieves a high level (>90%) with 1% of ODA concentration in DES phase (Supplementary Fig. 9a). As an acid acceptor, 0.2% of NaOH in the DES solution plays an essential role in the membrane preparation (Supplementary Fig. 9b).



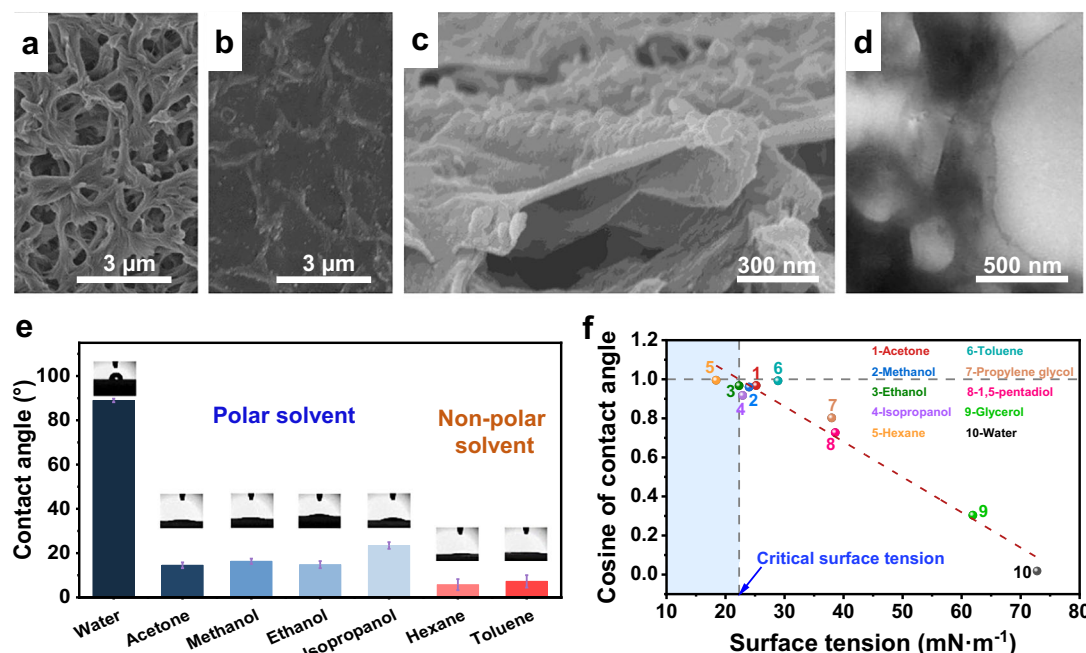


**Fig. 2 | Membrane morphologies and surface properties.** **a, b** SEM images of the surface of Nylon substrate and ODA/TMC TFC membrane. **c, d** SEM and TEM images of the cross-section of ODA/TMC TFC membrane. **e, f** Contact angles and Zisman plot for the ODA/TMC TFC membrane.

The optimal ODA/TMC TFC membrane exhibits a steep solute rejection profile, as shown in Fig. 3b. The dye molecules with molecular weight >600 Da could be effectively rejected (Supplementary Table 3, Fig. 10). Notably, little or no dye deposition was observed on membrane surfaces for both positively and negatively charged dyes, suggesting that the primary mechanism of dye separation in ODA/TMC TFC membranes is rejection rather than adsorption (Supplementary Fig. 11). As an indicator for molecular separation capability of the membrane, the molecular weight retention onset (MWRO at 10% rejection) and cutoff (MWCO at 90% rejection) are determined to be ~540 Da and 600 Da, respectively. The ultralow value of 60 Da for the difference between MWRO and MWCO, offers the precise molecular sieving capability, suggesting the uniform pore architecture of PA network. Observed from Fig. 3c, the clear separation of a mixed solution of bromocresol purple (BCP, 540.2 Da) and methyl blue (BS, 799.8 Da) is achieved based on accurate shape selectivity of ODA/TMC TFC membrane. The BCP molecules could easily pass through the membrane with a low rejection of 10.1%, while BS molecules are almost retained with a high retention of 97.1%.

To thoroughly appraise the potential of ODA/TMC TFC membrane for OSN application, the permeance of the membrane towards various organic solvents was measured at ambient temperature and displayed in Fig. 3d. Impressively, ultrahigh fluxes are achieved for both polar and non-polar solvents, i.e., polar acetone (88.1 L h<sup>-1</sup> m<sup>-2</sup> bar<sup>-1</sup>) and methanol (36.6 L h<sup>-1</sup> m<sup>-2</sup> bar<sup>-1</sup>), non-polar hexane (56.6 L h<sup>-1</sup> m<sup>-2</sup> bar<sup>-1</sup>), cyclohexane (17.9 L h<sup>-1</sup> m<sup>-2</sup> bar<sup>-1</sup>) and toluene (10.2 L h<sup>-1</sup> m<sup>-2</sup> bar<sup>-1</sup>). It is worthy of noting the ODA/TMC TFC membrane features prominently in a fast transport for organic solvents across a wide range of polarity, while the traditional PA membrane is permeable to only polar solvents but essentially impermeable to nonpolar solvents.

The ultrahigh permeability of the OSN membrane to both polar and non-polar organic solvents stems from its precisely engineered molecular architecture, achieved through the strategic combination of a contorted diphenyl ether-based amine monomer and a carefully controlled IP process at the DES/alkane interface. Primarily, a delicate equilibrium of hydrophilicity-hydrophobicity of ODA/TMC network is achieved. This balance not only enhances the membrane and solvent affinity to promote molecular entry into the pores, but also facilitates

the formation of active dual channels for solvent molecules' transport<sup>2,6</sup>. Regarding the hierarchical architecture of ODA/TMC network, hydrophilic domains are formed by residual hydrolyzed carboxyl groups and amide groups, while the hydrophobic regions are strengthened via the incorporation of additional benzene rings from ODA, compared with conventional PA from MPD/TMC. The solvent molecules would preferentially transport through those domains with certain affinity. As calculated in Supplementary Tables 4–6, the low values of the solubility parameter differences ( $\Delta\delta_{sp}$ ) between ODA/TMC polyamide and solvents witness the intensive solvent-polymer interactions towards both polar solvents (methanol and acetone) and non-polar solvents (hexane and toluene). Furthermore, the degree of the interactions between the polymer and the solvents were qualitatively estimated by the chi ( $\chi$ ) parameter according to Flory–Huggins theory (Supplementary Table 7)<sup>22</sup>. For both  $\chi$  values of PA-methanol and PA-acetone between 0.5 and 2, the strong interactions between PA and methanol (or acetone) are favorable to the solvent permeability, without causing plethoric swelling of the membrane. Meanwhile, the relative small interactions between PA and non-polar solvent (hexane and toluene) are indicated by higher  $\chi$  values. Moreover, the ultrathin ODA/TMC layer with enhance microporosity and interconnectivity provides transport superhighways for solvent molecules, promoting the solvent migration<sup>17,23,24</sup>. These results reveal the microporous Janus-like structure of ODA/TMC membrane is powerful for efficient polar and non-polar solvent transport.

The solvent permeance decreases along with the increment of viscosity, and an obvious deviation is also observed from the inverse linear relationship (Supplementary Fig. 12a). Finally, a linear fit ( $R^2 = 0.923$ ) is found between the permeance and a combined solvent parameters  $\delta_0 \eta^{-2} d_m^{-1}$ , where  $\delta_0$ ,  $\eta$ ,  $d_m$  are the Hansen solubility parameter, solvent viscosity, and solvent molecular diameter, respectively (Fig. 3d, Supplementary Table 8). That is to say, solvent transport through the ODA/TMC membrane is governed not only by solvent viscosity but also significantly influenced by solvent-polymer interactions and steric hindrance effects. This transport behavior markedly differs from that observed in conventional polyamide membranes, revealing distinct structure-property relationships<sup>1</sup>. It is speculated that the strong solvent-polyamide interactions for both polar and

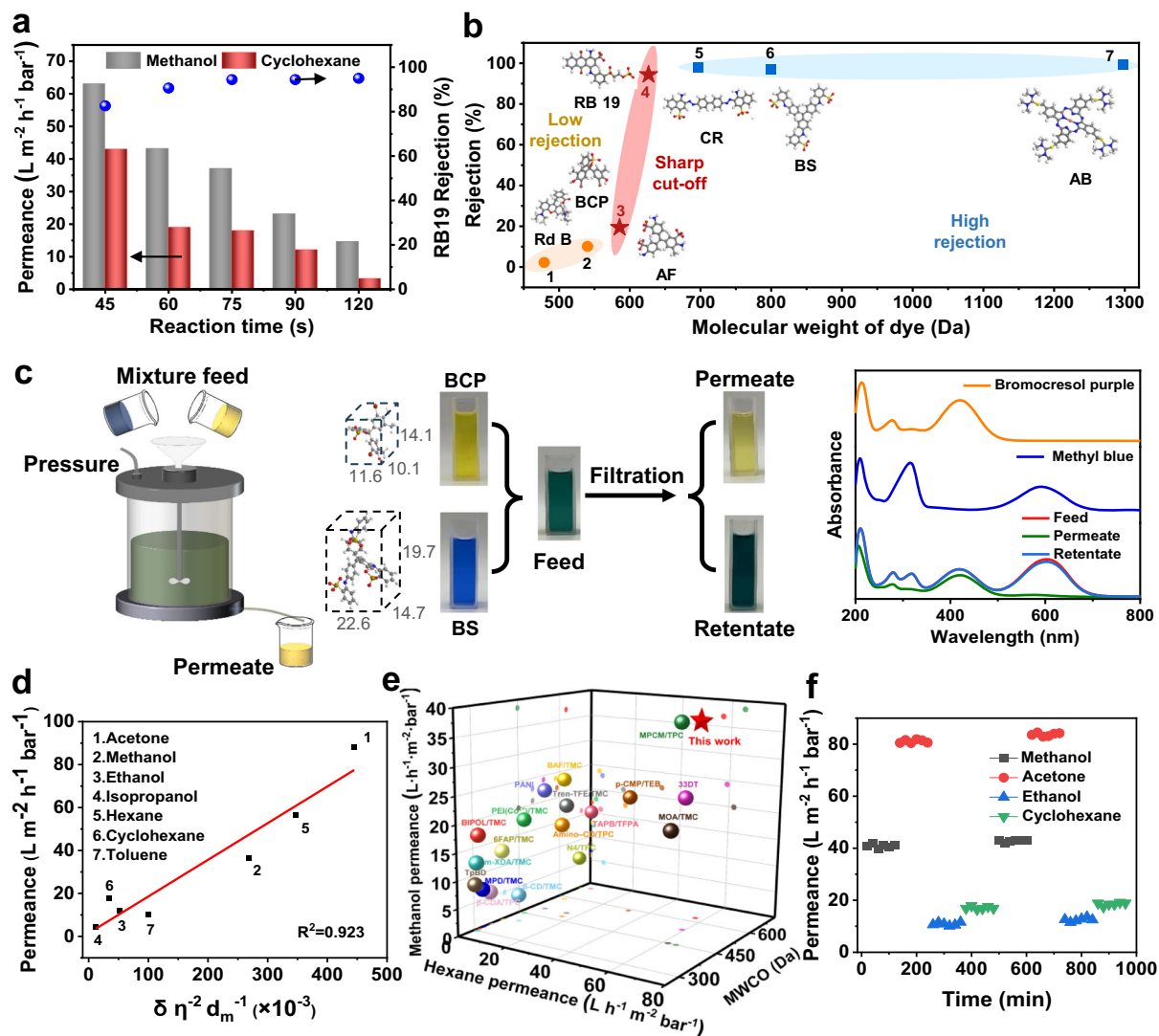


**Fig. 3 | Nanofiltration performance.** **a** Effect of reaction time on the membrane performance. **b** Rejection of the ODA/TMC TFC membrane for dyes with different sizes and molecular weights. **c** Schematic illustration of the filtration of bromocresol purple and methyl blue mixture using ODA/TMC TFC membrane, and corresponding UV-Vis absorption spectra. **d** Relationship between permeance and the

combined solvent property for ODA/TMC TFC membrane. **e** A comparison between the ODA/TMC TFC membrane and previously reported membranes in terms of the solvent permeance (methanol and hexane) and MWCO. **f** Permeance of ODA/TMC TFC membrane for different solvents.

non-polar solvents make unique impact on the flow behavior in solution-diffusion model by modulating both diffusivity and solubility parameters.

Figure 3e demonstrates the comparison with state-of-the-art OSN membranes reported, the ODA/TMC TFC membrane gives significant advantage in both high permeance for polar/nonpolar solvents and comparable MWCO for small organic solutes, breeding a promising candidate for industrial OSN process (Supplementary Table 9)<sup>2,5,6,8,10,11,13,15,17,25–32</sup>. Noting that, compared with commercially available OSN membrane e.g., DuraMem 500, the methanol permeance of ODA/TMC TFC membrane is six times higher than that of DuraMem 500 ( $\sim 5 \text{ L h}^{-1} \text{m}^{-2} \text{bar}^{-1}$ ), and the permeance to hexane is approximately ten times that of DuraMem 500 ( $\sim 5.52 \text{ L h}^{-1} \text{m}^{-2} \text{bar}^{-1}$ )<sup>21,22</sup>.

The stability of ODA/TMC TFC membrane was also measured. The solvent fluxes of the membrane exhibit an increase proportionally to the applied pressure from 1 to 8 bar (Supplementary Fig. 13),

confirming the stable microstructure of the permselective PA layer. Furthermore, as shown in Fig. 3f, after consecutive operation by alternating methanol, acetone, ethanol and cyclohexane for 16 h, the well-maintained solvent permeance reveals the robustness and long-term operation endurance of membrane. The ODA/TMC TFC membrane exhibits an excellent stability in both morphology and performance after the immersion in various organic solvents with a wide range of polarity for 4 days (Supplementary Fig. 14).

### Mass transport behavior and molecular dynamics simulation

Along with the development of the OSN membrane, various theoretical models have been piloted to interpret the organic solvent transport through those membranes<sup>33</sup>. The pore flow and solution-diffusion model are commonly used. The pore flow model, which utilizes Hagen–Poiseuille equation to represent viscous flow, considers only the solvent's viscosity as a governing factor<sup>34</sup>. This model is generally

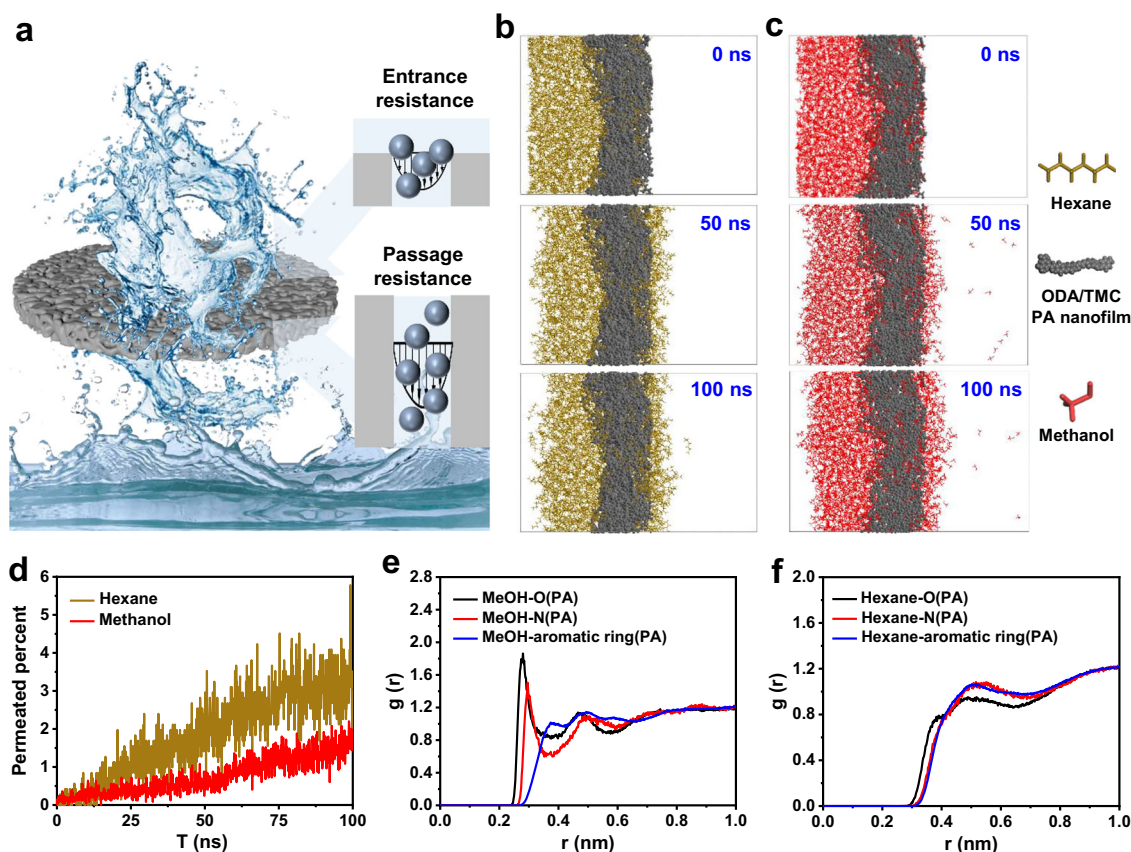


**Fig. 4 | Solvent transport behaviors.** **a** Representation of pressure-driven flow through ODA/TMC membrane. **b, c** Snapshot of the permeation simulation of hexane and methanol through ODA/TMC. **d** Permeated percentage of methanol and hexane through ODA/TMC. **e, f** RDF of methanol and hexane in ODA/TMC.

applicable for describing ultrafiltration processes but is inadequate for capturing the behavior of nanofiltration. Indeed, the pore flow model does not align well with the observed performance of ODA/TMC membrane (Supplementary Fig. 12a). The solution-diffusion model has been primarily applied to explain the mass transport mechanism in dense PA membranes. This model suggests that permeation process involves the dissolution of solvent molecules into the membrane pores followed by their diffusion through the membrane. However, it remains challenging to clearly differentiate the individual contribution of the solubility and diffusivity, leading to the accuracy limitation of solution-diffusion model<sup>35</sup>. Furthermore, several resistances-in-series models, that assume the overall resistances for the permeation could be deduced by summing the individual resistances encountered in the membranes, have been constructed<sup>33,36</sup>.

To vividly illustrate the mass transport process, the schematic representation of solvent flow through the membrane is provided in Fig. 4a. Herein, the total transport resistance is attributed to the resistances at the membrane surface and across the pores, with negligible contribution from the porous ultrafiltration substrate. Dagan' model, which integrates Sampson's pore entrance resistance and Hagen–Poiseuille's pore passage resistance to describe the overall transport resistances, is firstly employed to analyze the mass transport of ODA/TMC nanofilm<sup>21,37</sup>. As shown in Supplementary Fig. 15, the higher thickness-to-pore radius aspect ratio reveals the domination of pore passage resistance in mass transport, but the influence of the entrance resistance needs to be valued for such an ultrathin dense membrane. In Dagan' model, only membrane's geometry factor and solvent's viscosity are considered, however, the effect of the solvent-membrane interactions could not be overlooked during the solvent permeation of ODA/TMC membrane, as discussed before.

Further, the affinity between the solvent liquids and ODA/TMC membrane surface was investigated by using Lucas–Washburn equation, which describes the capillarity force (pressure) as  $2\gamma \cos\theta/R$ , where the contact angle between the liquid and solid ( $\theta$ ), liquid surface tension ( $\gamma$ ) and pore radius ( $R$ ) are directly correlated with it. The positive contact angle cosine values and corresponding positive capillary driving forces indicate strong affinity between the ODA/TMC membrane surface and various solvents, including non-solvents. This favorable interaction promotes spontaneous penetration of solvent molecules into membrane pores through capillary action, thereby reducing entrance resistance and significantly enhancing liquid transport efficiency<sup>38–40</sup>.

The continuous solvent flow was simulated by molecular dynamics, to rationalize the mass transport across the ODA/TMC matrix (Fig. 4b–f, Supplementary Table 10). As schemed in Fig. 4b–d, the hexane exhibits a faster transport rate than methanol in the ODA/TMC membrane, which is in line with the experimental permeance. The radial distribution function (RDF) values of methanol and hexane in ODA/TMC membrane during solvent permeation were elucidated. Observed from Fig. 4e, the oxygen and nitrogen atoms of PA membrane are the preferential sites for the interactions towards methanol molecules, with main peaks appear at a low value of  $\sim 0.3$  nm, revealing quite strong attractive interactions. And the RDF between the aromatic rings of PA membrane and the methanol molecules presents a far peak at  $\sim 0.4$  nm, as a result of a weak attractive interaction. The strong affinity between methanol and PA membrane, ascribed to the formation of multiple hydrogen bonds, leading to a significant confinement of methanol molecules in the PA matrix. In contrast to the robust interactions with methanol, the less favorable interactions are found between the hexane and PA, as all the first main peaks located at



~0.4 nm, and the relative high hexane affinity with the aromatic ring arise. Consequently, the effective interaction strength for methanol is higher than hexane. In addition to solvent viscosity, specific solvent-membrane interactions also substantially influence transmembrane transport properties. Therefore, the MSD sequence of the hexane is found slightly higher than methanol across the ODA/TMC membrane, with a much smaller viscosity ( $\eta_{\text{Hexane}}$  (0.29 mPa s) vs  $\eta_{\text{Methanol}}$  (0.54 mPa s)) (Supplementary Fig. 16).

## Discussion

A facile strategy for the preparation of OSN membranes with an ultrathin polyamide layer featuring a Janus-like microporous microstructure, was put forward. The target membrane was obtained through the interfacial polymerization of ODA and TMC at a DES/alkane interface. By leveraging the unique properties of DES, including its strong solubility, high viscosity and interfacial stability, the interfacial polymerization process is precisely controlled. In this anhydrous system free from water-induced side reactions, the finely regulated diffusion kinetics ensures the formation of a highly cross-linked polyamide layer (~12 nm) with uniform pore structure. The incorporation of contorted ODA diamine monomer containing diphenyl ether groups yields a PA architecture with enhanced interconnectivity and microporosity, providing abundant transport channels. Moreover, the balanced distribution of hydrophilic and hydrophobic domains promotes high surface affinity, establishing dual transport pathways for both polar and non-polar solvents, e.g., methanol and hexane permeance reach as high as 36.6 and 56.6 L m<sup>-2</sup> h<sup>-1</sup> bar<sup>-1</sup>, respectively. Notably, the ODA/TMC TFC membrane also exhibits remarkable molecular sieving capability, structural stability and operational durability. The molecular transport mechanism was further elucidated by systematically analyzing solvent-polymer interactions during the solvent permeation process. This work provides fundamental insights for developing advanced OSN membranes for applications across diverse solvent systems, highlighting the importance of rational molecular design and tailored interfacial polymerization.

## Method

### Materials

Nylon porous membranes (pore size: 0.22 μm) were provided by Delvst lab. 1,3,5-Benzenetricarbonyl chloride (TMC, purity ~98%) was purchased from Energy Chemical. Choline chloride (ChCl, purity ≥98%), 4,4'-diaminodiphenyl ether (ODA, purity ≥98%) and Congo red (purity ≥98%) were bought from Aladdin. Rhodamine B (purity ~99%) was provided by Rhawn. Acid Fuchsin (purity ≥70%) was obtained from Shanghai yuanye Bio-Technology Co., Ltd. Reactive Blue 19 (purity ~65%) was purchased from Sigma-Aldrich. Alcian blue 8GX (purity ~80%) was bought from BOSF Co., Ltd. Methyl blue was bought from Shanghai Macklin Biochemical Co., Ltd. Bromocresol purple (purity ≥98%), crystal violet (purity ≥90%), Janus green (purity ~65%), ethylene glycol (EG, purity ≥99.5%), cyclohexane (purity ≥99.7%), hexane (purity ~99%), toluene (purity ≥99.5%), isopropanol (purity ≥99.7%), ethanol (purity ≥99.5%), acetone (purity ≥99.5%) and methanol (purity ≥99.5%) were obtained from Shanghai Titan Scientific Co., Ltd. All of the chemicals were used without further purification and deionized (DI) water was used through all experiments.

### Preparation of deep eutectic solvent

The DES was made from EG and ChCl. EG and ChCl were mixed at a molar ratio of 17:3 and kept stirring at 70 °C to receive a homogeneous colorless liquid.

### Preparation of ODA/TMC TFC membrane

The ODA/TMC TFC membrane was prepared through interfacial polymerization (IP) in DES/cyclohexane system. DES solution containing a certain concentration of ODA and NaOH was poured onto the

Nylon substrate settled in the vacuum filter flask, and the solution was filtered through the substrate under a pressure of 0.1 MPa. Subsequently, TMC/cyclohexane solution was slowly poured to conduct the interfacial polymerization process for a certain time. After removing TMC solution, the membrane was immersed in cyclohexane for 1 min and heat-treated at 60 °C for 15 min, followed by DI water washing. The ODA/TMC TFC membrane was finally obtained. The free-standing ODA/TMC nanofilm was collected from the DES/cyclohexane interface using the same IP parameters.

### Characterizations

The viscosity of the DES was measured by a viscometer (DV2TLV). Wilhelmy plate method was used to test the surface tension and the interfacial tension by force tensiometer (K100). The chemical structure of ODA/TMC sample was characterized by Fourier transform infrared spectroscopy (FTIR, Nicolet-iS50), and X-ray photoelectron spectrometer (XPS, Scientific K-Alpha) was used for elementary analysis. Small-angle X-ray scattering (SAXS) experiments were conducted using the laboratory-based SAXS-WAXS beamline, KWS-X (XENOCSS XUESS 3.0 XL, France), at JCMS-MLZ in Garching, Germany. Surface and cross-sectional morphologies of ODA/TMC TFC membranes were observed by a field emission scanning electron microscopy (FESEM, SU8230). Transmission electron microscope (TEM, JEM-2100) was used to study the cross-sectional structure of membrane sample. Small pieces of ODA/TMC TFC membrane were embedded in epoxy resin, cut by ultramicrotome and placed on copper grids, to prepare membrane sample for TEM imaging. Atomic force microscopy (AFM, Dimension Icon) was carried out to measure the thickness of the ODA/TMC free-standing nanofilms collected on clean silicon wafer. The contact angles were primarily used to characterize the affinity between the membranes and various solvents, and determined by contact angle instrument (Biolin). The streaming potential values of ODA/TMC TFC membrane were measured by Electrokinetic analyzer (Anton Paar, SurPASS 3) using 1 mM KCl electrolyte solution at a pH range of 3–11. The thermal stability test of ODA/TMC TFC membrane was conducted on a thermogravimetric analyzer (TGA, STA8000), at a rate of 20 °C/min in a nitrogen atmosphere. CO<sub>2</sub> sorption isotherm was measured by Brunauer-Emmett-Teller (BET, Autosorb IQ), to analyze the specific surface area and pore size distribution of polyamide nanofilms.

### Nanofiltration performance tests

The nanofiltration experiments were performed on a lab-scale dead-end apparatus at a pressure of 2 bar, and the effective test area for membrane was 4.9 cm<sup>2</sup>. Before measurement, all the membranes were pretreated for 10 min under 2 bar pressure. The solvent permeance (P, L h<sup>-1</sup> m<sup>2</sup> bar<sup>-1</sup>) was calculated based on the following Eq. 1:

$$P = V / (A \cdot \Delta t \cdot \Delta P) \quad (1)$$

where  $V$  (L) represents the volume of collected permeate solution during filtration time  $\Delta t$  (h),  $A$  and  $\Delta P$  represents the effective membrane area (m<sup>2</sup>) and the applied pressure (bar), respectively.

The solute rejection ( $R$ ) was calculated according to Eq. 2:

$$R = (1 - C_p / C_f) \times 100\% \quad (2)$$

where  $C_p$  and  $C_f$  represent the concentration of permeate and feed solutions, respectively. The concentrations of various dyes in feed solution were 50 ppm. The dye concentrations in the feed and permeate solutions were determined by a UV-vis spectrometer (PerkinElmer, Lambda 950).

### Calculation of electrostatic potential distribution

Geometry optimization was firstly operated for all molecules using density functional theory (DFT) at the M06-2X level of theory with

6-31G(d') basis set. The corrections for solvation energy and Grimme's D3 (zero-damping) dispersion were included. The distribution of ESP and extreme points at the molecular van der Waals surface of all amine monomers were calculated by Multiwfn 3.7 program. Gaussian 09 software package was employed for all DFT calculations. Additionally, the isosurface maps of the amine monomers were visualized by VMD 1.9.4 software.

### Calculation of monomer partition coefficients in different solvent systems

The partition coefficient could offer valuable message for the monomer diffusion mechanism in IP system. The partition ratio, which was usually expressed in the form of the distribution coefficient ( $\log P_{A/B}$ ), could be obtained from the free energy difference in two solvents as the following Eq. 3:

$$\log P_{A/B} = \frac{\Delta G_{\text{solv}}(A) - \Delta G_{\text{solv}}(B)}{2.303RT} = \frac{E(A) - E(B)}{2.303RT} \quad (3)$$

where,  $\log P_{A/B}$  is the partition coefficient of the solute between solvent A and solvent B.  $\Delta G_{\text{solv}}$  is the free energy of the solute in the corresponding solvent,  $E$  is the single point energy,  $R$  is the ideal gas constant ( $8.314 \text{ J mol}^{-1} \text{ K}^{-1}$ ), and  $T$  is the temperature (K), calculated using SMD model at M06-2X level of theory with the 6-31G(d) basis set.

### Calculation of mean square displacement of amine monomer in different solvents

MD simulations were carried out to reveal the transport of amine monomer molecules, using Materials Studio 2020 and COMPASS II force field. Amorphous box ( $26.1 \text{ \AA}$  side length) containing 6 monomer molecules and 7 DES molecules (including 21 ChCl and 119 EG) molecules was constructed in the amorphous cell module. Geometric optimization and annealing was performed, followed by NPT and NVT for 100 ps each with a time step of 1 fs. The mean square displacement (MSD) curves could be obtained for analyzing.

### Calculation of fractional free volume (FFV) of polyamide structure

Molecular dynamics simulations were performed using Materials Studio 2020 with the COMPASS II force field. An amorphous cell with ODA (60) and TMC (40) units was built using the amorphous cell module. The geometry optimization and annealing were applied to the cell for energy minimum. NPT and NVT was performed sequentially, each for 100 ps, with the temperature and pressure set to 295 K and 8 bar, respectively. The velocity Verlet algorithm was used to integrate the equations of motion with a time step 1 fs. The long-range Coulombic interactions were calculated with a cutoff distance of  $12.5 \text{ \AA}$ . The FFV of polymer was estimated by the following Eq. 4:

$$\text{FFV} = V_f / (V_f + V_0) \quad (4)$$

where  $V_f$  and  $V_0$  are the free volume and occupied volume, respectively. The values of  $V_f$  and  $V_0$  are explored using probe with radius of  $1 \text{ \AA}$ , synchronously giving the morphology of voids in aggregate.

### Calculation of translational dynamics of the solvent molecules across the membrane

Atomistic molecular dynamic simulations were conducted using GROMACS simulation package (version 2020.6) with the General Amber force field (GAFF2). The polymer was initially built in the amorphous builder of the Materials Studio software, and the final structure was exported into the Gromacs software. The polyamide system was first equilibrated for 20 ns at an elevated temperature of 500 K to relax the structure and facilitate expansion along the Z-axis of

the matrix. Subsequently, two solvents (hexane and methanol) were individually introduced on one side of the polyamide membrane. To prevent solvent molecules from crossing to the other side due to periodic boundary conditions, an implicit wall was placed at the bottom of the simulation box. After energy minimization (1000 steps), the systems were further equilibrated for 5 ns to ensure structural relaxation before initiating production runs of 100 ns under the canonical ensemble. The temperature was maintained at 298 K using the Nose-Hoover method and the pressure was controlled at 1 atm using the Parrinello-Rahman method. For non-bonded interactions, a cutoff distance of  $1.2 \text{ nm}$  was applied, while long-range electrostatic interactions were treated using the Particle Mesh Ewald method with a Fourier spacing of  $0.1 \text{ nm}$ . All covalent bonds involving hydrogen atoms were constrained using the LINCS algorithm.

### Statistics and reproducibility

All experiments were repeated independently with similar results for at least three times.

### Data availability

All data supporting the findings of this study are available within this article and Supplementary Information or from the corresponding author upon request. The data generated in this study are provided in the Supplementary Information.

### References

- Karan, S., Jiang, Z. & Livingston, A. G. Sub-10 nm polyamide nanofilms with ultrafast solvent transport for molecular separation. *Science* **348**, 1347–1351 (2015).
- Liu, J., Hua, D., Zhang, Y., Japip, S. & Chung, T.-S. Precise molecular sieving architectures with Janus pathways for both polar and non-polar molecules. *Adv. Mater.* **30**, 1705933 (2018).
- Shi, G. M. et al. Recent progress of organic solvent nanofiltration membranes. *Prog. Polym. Sci.* **123**, 101470 (2021).
- Sengupta, B. et al. Carbon-doped metal oxide interfacial nanofilms for ultrafast and precise separation of molecules. *Science* **381**, 1098–1104 (2023).
- Li, S. et al. Hydrophobic polyamide nanofilms provide rapid transport for crude oil separation. *Science* **377**, 1555–1561 (2022).
- Hu, Y. X. et al. Two copolymer-grafted silica stationary phases prepared by surface thiol-ene click reaction in deep eutectic solvents for hydrophilic interaction chromatography. *J. Chromatogr. A* **1609**, 460446 (2020).
- Lee, T. H., Balcik, M., Wu, W.-N., Pinnau, I. & Smith, Z. P. Dual-phase microporous polymer nanofilms by interfacial polymerization for ultrafast molecular separation. *Sci. Adv.* **10**, eadp6666 (2024).
- Jiang, Z. et al. Aligned macrocycle pores in ultrathin films for accurate molecular sieving. *Nature* **609**, 58–64 (2022).
- Zheng, X. et al. Modulating hydrophobicity of composite polyamide membranes to enhance the organic solvent nanofiltration. *Sep. Purif. Technol.* **223**, 211–223 (2019).
- Huang, T. et al. Molecularly-porous ultrathin membranes for highly selective organic solvent nanofiltration. *Nat. Commun.* **11**, 5882 (2020).
- Huang, T., Puspasari, T., Nunes, S. P. & Peinemann, K.-V. Ultrathin 2D-layered cyclodextrin membranes for high-performance organic solvent nanofiltration. *Adv. Funct. Mater.* **30**, 1906797 (2020).
- Xu, G. et al. Influence of polar solvent in formation and organic solvent separation performance of novel fluorine-containing polyamide membranes. *J. Membr. Sci.* **706**, 122969 (2024).
- Li, S.-L. et al. 2,2'-Biphenol-based ultrathin microporous nanofilms for highly efficient molecular sieving separation. *Angew. Chem. Int. Ed.* **61**, e202212816 (2022).



14. Wang, S. et al. Highly porous ultrathin polyamide membranes for fast separation of small molecules from organic solvents. *J. Membr. Sci.* **675**, 121540 (2023).
15. Li, X. et al. Polycage membranes for precise molecular separation and catalysis. *Nat. Commun.* **14**, 3112 (2023).
16. Liu, S.-H. et al. Sub-8 nm networked cage nanofilm with tunable nanofluidic channels for adaptive sieving. *Nat. Commun.* **15**, 2478 (2024).
17. Liang, B. et al. Microporous membranes comprising conjugated polymers with rigid backbones enable ultrafast organic-solvent nanofiltration. *Nat. Chem.* **10**, 961–967 (2018).
18. Lu, T. & Chen, F. Multiwfn: A multifunctional wavefunction analyzer. *J. Comput. Chem.* **33**, 580–592 (2012).
19. Schubert, K. V., Strey, R., Kline, S. R. & Kaler, E. W. Small angle neutron scattering near Lifshitz lines: Transition from weakly structured mixtures to microemulsions. *J. Chem. Phys.* **101**, 5343–5355 (1994).
20. Machado, D. R., Hasson, D. & Semiat, R. Effect of solvent properties on permeate flow through nanofiltration membranes-Part II. Transport model. *J. Membr. Sci.* **166**, 63–69 (2000).
21. Shevate, R. & Shaffer, D. L. Large-area 2D covalent organic framework membranes with tunable single-digit nanopores for predictable mass transport. *ACS Nano* **16**, 2407–2418 (2022).
22. Ghazali, N. F., Hanim, K. M., Pahlawi, Q. A. & Lim, K. M. Enrichment of carotene from palm oil by organic solvent nanofiltration. *J. Am. Oil Chem. Soc.* **99**, 189–202 (2022).
23. Jimenez-Solomon, M. F., Song, Q., Jelfs, K. E., Munoz-Ibanez, M. & Livingston, A. G. Polymer nanofilms with enhanced microporosity by interfacial polymerization. *Nat. Mater.* **15**, 760–767 (2016).
24. Ali, Z. et al. Finely tuned submicroporous thin-film molecular sieve membranes for highly efficient fluid separations. *Adv. Mater.* **32**, 2001132 (2020).
25. Sun, Y. et al. Rigid twisted structured PA membranes for organic solvent nanofiltration via co-solvent assisted interfacial polymerization. *J. Membr. Sci.* **666**, 121179 (2023).
26. Alduraiei, F., Kumar, S., Liu, J., Nunes, S. P. & Szekely, G. Rapid fabrication of fluorinated covalent organic polymer membranes for organic solvent nanofiltration. *J. Membr. Sci.* **648**, 120345 (2022).
27. He, P. et al. In-situ growth of double-layered polyaniline composite membrane for organic solvent nanofiltration. *Chem. Eng. J.* **420**, 129338 (2021).
28. Fu, W. et al. Polyamide composite membrane with 3D honeycomb-like structure via acetone-regulated interfacial polymerization for high-efficiency organic solvent nanofiltration. *J. Membr. Sci.* **679**, 121711 (2023).
29. Yao, A. et al. Flexible covalent organic network with ordered honeycomb nanoarchitecture for molecular separations. *ACS Nano* **17**, 22916–22927 (2023).
30. Zheng, D. et al. Polyamide composite membranes for enhanced organic solvent nanofiltration performance by metal ions assisted interfacial polymerization method. *AIChE J.* **69**, e17896 (2023).
31. Jin, C.-G. et al. Fabrication of coffee-ring nanostructured membranes for organic solvent nanofiltration. *Angew. Chem. Int. Ed.* **63**, e202405891 (2024).
32. Mi, K., Xiong, S., Lu, Y. & Wang, Y. Precise fabrication of robust conjugated microporous polymer membranes via oxidative molecular layer deposition for efficient organic solvent nanofiltration. *Chem. Mater.* **36**, 7069–7078 (2024).
33. Marchetti, P., Solomon, M. F. J., Szekely, G. & Livingston, A. G. Molecular separation with organic solvent nanofiltration: a critical review. *Chem. Rev.* **114**, 10735–10806 (2014).
34. Karan, S., Samitsu, S., Peng, X., Kurashima, K. & Ichinose, I. Ultrafast viscous permeation of organic solvents through diamond-like carbon nanosheets. *Science* **335**, 444–447 (2012).
35. Shin, M. G. et al. Solvent transport model for polyamide nanofilm membranes based on accurate Hansen solubility parameters. *J. Membr. Sci.* **674**, 121505 (2023).
36. Marchetti, P., Butté, A. & Livingston, A. G. An improved phenomenological model for prediction of solvent permeation through ceramic NF and UF membranes. *J. Membr. Sci.* **415**, 444–458 (2012).
37. Buchheim, J., Schlichting, K.-P., Wyss, R. M. & Park, H. G. Assessing the thickness-permeation paradigm in nanoporous membranes. *ACS Nano* **13**, 134–142 (2019).
38. Dimitrov, D. I., Milchev, A. & Binder, K. Capillary rise in nanopores: molecular dynamics evidence for the Lucas-Washburn equation. *Phys. Rev. Lett.* **99**, 054501 (2007).
39. Shi, D. et al. Intercrystalline channels at subnanometer scale for precise molecular nanofiltration. *J. Am. Chem. Soc.* **145**, 15848–15858 (2023).
40. Fan, H. et al. The physical basis for solvent flow in organic solvent nanofiltration. *Sci. Adv.* **10**, eado4332 (2024).

## Acknowledgements

The authors gratefully acknowledge the financial support of the National Natural Science Foundation of China (NSFC) (No. 52433003 received by P. W.). We are very grateful for the kind support from National Innovation Center of Advanced Dyeing and Finishing Technology. We also greatly appreciate Prof. Pengfei Zhang from Donghua University, China, for the kind help regarding the analysis of MD simulation.

## Author contributions

H.W. and P.W. designed and directed the project. H.W. and Y.X. carried out the experiments, analyzed the data and wrote the paper. Q.T. operated the TEM measurement and B.W. performed the SAXS test. All authors discussed the results and revised the manuscript.

## Competing interests

The authors declare no competing interests.

## Additional information

**Supplementary information** The online version contains supplementary material available at <https://doi.org/10.1038/s41467-025-63663-0>.

**Correspondence** and requests for materials should be addressed to Huiqing Wu or Peiyi Wu.

**Peer review information** *Nature Communications* thanks P.Z. Çulfaz-Emecen, Marina Guenza and the other, anonymous, reviewer(s) for their contribution to the peer review of this work. A peer review file is available.

**Reprints and permissions information** is available at <http://www.nature.com/reprints>

**Publisher's note** Springer Nature remains neutral with regard to jurisdictional claims in published maps and institutional affiliations.

**Open Access** This article is licensed under a Creative Commons Attribution-NonCommercial-NoDerivatives 4.0 International License, which permits any non-commercial use, sharing, distribution and reproduction in any medium or format, as long as you give appropriate credit to the original author(s) and the source, provide a link to the Creative Commons licence, and indicate if you modified the licensed material. You do not have permission under this licence to share adapted material derived from this article or parts of it. The images or other third party material in this article are included in the article's Creative Commons licence, unless indicated otherwise in a credit line to the material. If material is not included in the article's Creative Commons licence and your intended use is not permitted by statutory regulation or exceeds the permitted use, you will need to obtain permission directly from the copyright holder. To view a copy of this licence, visit <http://creativecommons.org/licenses/by-nc-nd/4.0/>.

© The Author(s) 2025